Check for updates

The influence of an ultra-high resistivity Ta underlayer on perpendicular magnetic anisotropy in Ta/Pt/Co/Pt heterostructures

Wei Zhang,[ab] Xiaoxiong Jia,[ab] Rui Wang,[a] Huihui Liu,[a] Zhengyu Xiao,[ab] Zhiyong Quan [ID] *[ab] and Xiaohong Xu [ID] *[ab]

Thin films with perpendicular magnetic anisotropy (PMA) play an essential role in the development of technologies due to their excellent thermal stability and potential application in devices with high density, high stability, and low energy consumption. Many studies have focused on the relationship between the resistivity of heavy metals and the PMA of the neighbouring magnetic metals in magnetic multi-layered films. However, reports on the effects of heavy metals non-adjacent to the magnetic metals on the PMA are rare. Herein, we demonstrate the influence of the heavy metal Ta underlayer non-adjacent to the magnetic Co layer on the PMA and thermal stability in the Ta/Pt/Co/Pt heterostructures. A type of amorphous Ta film having an ultra-high resistivity ($\rho_{max} = 3.9 \times 10^5$ μΩ cm) was optimized by DC sputtering at a high sputtering Ar pressure, low sputtering power, and large target-to-substrate distance. The value of resistivity is three orders of magnitude higher than that of the β-Ta underlayer. We found that this special Ta underlayer can effectively improve the PMA and thermal stability of the magnetic Co layer based on the anomalous Hall and planar Hall effect measurements. The maximum magnetic anisotropic field reaches 1.1 T at a low temperature. It is very likely that the ultra-high resistivity leads to the increase in the additional electron scattering in the Ta/Pt interface, while the latter results in the enhancement of the PMA and thermal stability in the structure. These results reveal the inherent relationship between the resistivity of the heavy metal underlayer and PMA, and provide a novel approach to improve the PMA and thermal stability of heavy metal/magnetic metal multi-layered films.

Introduction

Thin films with perpendicular magnetic anisotropy (PMA) play an essential role in the development of technologies in the field of modern magnetics. Due to their excellent thermal stability and potential applications in ultra-high-density devices, they have garnered strong research interests.[1–5] PMA is a notable behavior that causes the magnetic moment of a magnetic material to be aligned perpendicular to the film plane, whereas the shape of the thin film usually makes the magnetic moment parallel to the film plane. Currently, PMA materials are widely applied in memory and logic devices.[6–9] Since the magnetic moment being perpendicular to the film plane is beneficial to the formation of smaller storage cells, the magnetic storage density can be increased. The PMA films can effectively

eliminate the restrictions on the area and shape imposed by the vortex rotation in the magnetic layer. Moreover, the competitions between PMA and other magnetic mechanisms (such as Dzyaloshinskii–Moriya interaction) can produce rich and novel chiral spin textures, such as magnetic skyrmions.[10] Therefore, the realization and modulation of PMA in ferromagnetic materials is of great significance.

Recently, current-induced magnetization switching has been realized in PMA heavy metal/magnetic metal multi-layered films, which has significantly reduced the critical switching current density and the power consumption of devices.[11–18] In general, heavy metal layers with high resistivity, which are directly adjacent to the magnetic metal layer, are utilized to improve the PMA, spin–orbit torque (SOT) and critical switching current density of multi-layers. For example, in tungsten/magnetic metal films, the high resistivity of β-W can significantly increase the effective magnetic anisotropic field (H_{an}), thus leading to a decrease in the critical switching current density and a significant increase in the spin Hall angle.[19–24] The same results were also reported for high resistivity β-Ta based multilayered film structures.[25–28] Moreover, the insertion of a non-magnetic layer between the heavy metal/magnetic metal

[a]Key Laboratory of Magnetic Molecules and Magnetic Information Materials of Ministry of Education, The School of Chemistry and Materials Science, Shanxi Normal University, Linfen 041004, China. E-mail: quanzy@sxnu.edu.cn; xuxh@sxnu.edu.cn

[b]Research Institute of Materials Science, Shanxi Normal University, Linfen 041004, China

layers will also affect the spin–orbit coupling (SOC) of the film interface, and an appropriate insertion layer can effectively improve the PMA and reduce the spin Hall current density.[29–32] However, there are few studies on the influence of the inserted heavy metal layer non-adjacent to the magnetic metals on PMA and SOT in the heavy metal/magnetic metal multi-layered films. In this study, the influence of the Ta underlayer inserted between the substrate and heavy metal/magnetic metal multi-layers on the PMA and thermal stability was investigated. A type of ultra-high resistivity Ta film was obtained *via* the optimization of the experimental conditions, and its maximum resistivity reaches 3.9×10^5 μΩ cm, which is three orders of magnitude higher than that of β-Ta. The anomalous and planar Hall effect measurements show that the Ta underlayer having ultra-high resistivity effectively improved the H_{an} and thermal stability of Ta/Pt/Co/Pt multi-layered films. The highest H_{an} is 1.1 T at a low temperature, which is far larger than that of the β-Ta underlayer samples. This study provides a novel approach to improve the PMA and thermal stability of the heavy metal/ magnetic metal multi-layered films.

Experimental method

Pt (5 nm)/Co (0.9 nm)/Pt (2 nm) (labeled as Pt/Co/Pt) and Ta (3 nm)/Pt (5 nm)/Co (0.9 nm)/Pt (2 nm) (labeled as Ta/Pt/Co/Pt) multi-layered films were prepared by DC sputtering on thermally oxidized Si substrates at room temperature. The base pressure of the sputtering system was 5×10^{-9} torr and the sputtering target-to-substrate distance was 25 cm. The Pt layers were grown at Ar pressure of 4 mTorr and sputtering power of 15 W; the Co layers were grown at Ar pressure of 20 mTorr and sputtering power of 80 W. A series of Ta films with 20 nm thicknesses were prepared by changing the sputtering Ar pressure (4–20 mTorr) and sputtering power (8–20 W). A standard four-point probe was used to test the resistivity of Ta films. It was found that the Ta films fabricated at a high power and low sputtering Ar pressure have relatively small resistivity in the range of $(2.3–3.6) \times 10^2$ μΩ cm, corresponding to the β-Ta phase.[28,29] Moreover, the Ta films prepared at a low power and high sputtering Ar pressure have ultra-high resistivity, and the maximum value reaches 3.9×10^5 μΩ cm. In order to clear the influence of resistivity on the PMA, two types of Pt/Co/Pt multi-layered films with a 3 nm Ta underlayer were investigated. The β-Ta and ultra-high resistivity Ta layers were prepared under the conditions: sputtering Ar pressure of 4 mTorr and sputtering power of 20 W; sputtering Ar pressure of 20 mTorr and sputtering power of 8 W, respectively. The two types of Ta/Pt/Co/Pt multi-layered films were labeled as Ta/Pt/Co/Pt-4 and Ta/Pt/Co/Pt-20 according to Ta layer's sputtering Ar pressure. A superconducting quantum interference device (SQUID) magnetometer was used to measure the in-plane and out-of-plane magnetic properties of the films. X-ray diffraction (XRD) was used to characterize the structure of the multi-layered films, and atomic force microscopy (AFM) was used to characterize the surface morphologies of the Ta films. Using standard photolithography and Ar ion etching, the samples were patterned into Hall bars with dimensions of 10×100 μm^2 for Hall voltage measurements. A physical property measurement system (PPMS) was used for the transport measurements at temperatures ranging from 10 K to 300 K. The Ar in the Ta film was investigated *via* X-ray photoelectron spectroscopy (XPS) using an Al Kα X-ray source. The Ta/Pt/Co/Pt-20 sample was annealed in a vacuum furnace at two different temperatures of 260 °C and 380 °C for 1 hour.[22]

Results and discussion

Fig. 1 shows the in-plane and out-of-plane magnetic hysteresis loops of the Pt/Co/Pt, Ta/Pt/Co/Pt-4, and Ta/Pt/Co/Pt-20 samples measured at room temperature. As can be seen that all the three samples exhibit PMA, which is related to the interfacial symmetry break and strong interface SOC of the heavy metals.[33,34] The insertion of the Ta underlayer not only relaxes the lattice mismatch between the substrate and the heavy metal Pt but also effectively improves the squareness ratio and coercivity of the out-of-plane hysteresis loops, as shown in the insets of Fig. 1. Fig. 1(c) shows that the squareness ratio of the Ta/Pt/Co/Pt-20 sample was close to 1, and the coercivity reaches 440 Oe. These values are obviously larger than that of the Pt/Co/Pt and Ta/Pt/Co/Pt-4 samples [see the insets of Fig. 1(a) and (b)]. The value of H_{an} can be roughly estimated using the difference between the out-of-plane and in-plane saturation fields.[35,36] In the case of Ta/Pt/Co/Pt-20, the value of $H_{an} = \sim 2700$ Oe is clearly higher than that of the Pt/Co/Pt ($H_{an} = \sim 1100$ Oe) and Ta/Pt/Co/Pt-4 ($H_{an} = \sim 1500$ Oe) samples (the quantitative analysis of H_{an} will be carried out in the next content). Thus, the PMA and thermal stability of the Pt/Co/Pt can be enhanced by inserting the ultra-high resistivity Ta underlayer. Here, two points should be noted: first, the thermal stability can be represented using the equation: $\Delta = E/k_B T$,[33,37] where $E = M_S H_{an} V/2$ is the energy barrier between the two magnetization states, M_S is the saturation magnetization, H_{an} is the anisotropy field, V is the volume of the ferromagnetic Co layer, k_B is the Boltzmann constant, and T is the temperature. In our experiments, the hysteresis loops of three types of multi-layered films at the same Co thickness (0.9 nm) were measured at same temperature; and the values of M_S are approximately equal. Thus, $\Delta \propto H_{an}$, indicating that the sample of Ta/Pt/Co/Pt-20 with larger H_{an} has higher thermal stability. Second, in order to prove the thermal stability of the Ta/Pt/Co/Pt-20 film, annealing was carried out at two different temperatures of 260 °C and 380 °C for 1 hour in a vacuum furnace at a base pressure of 2.0×10^{-6} torr.[38] The out-of-plane hysteresis loops are shown in Fig. 1(d). The square loops indicate that strong PMA and high thermal stability of the Ta/Pt/Co/Pt-20 film can be maintained, even after annealing at 380 °C. This means that the thermal stability of the Ta/Pt/Co/Pt-20 film is far greater than that reported in previous publications.[39,40]

The following analysis will focus on the differences between Ta/Pt/Co/Pt-4 and Ta/Pt/Co/Pt-20 from two aspects: (i) the resistivity of the 20 nm Ta sample prepared at a sputtering Ar pressure of 4 mTorr and a sputtering power of 20 W is 2.3×10^2 μΩ cm, which belongs to β-Ta; however, the 20 nm Ta sample fabricated at a sputtering Ar pressure of 20 mTorr and
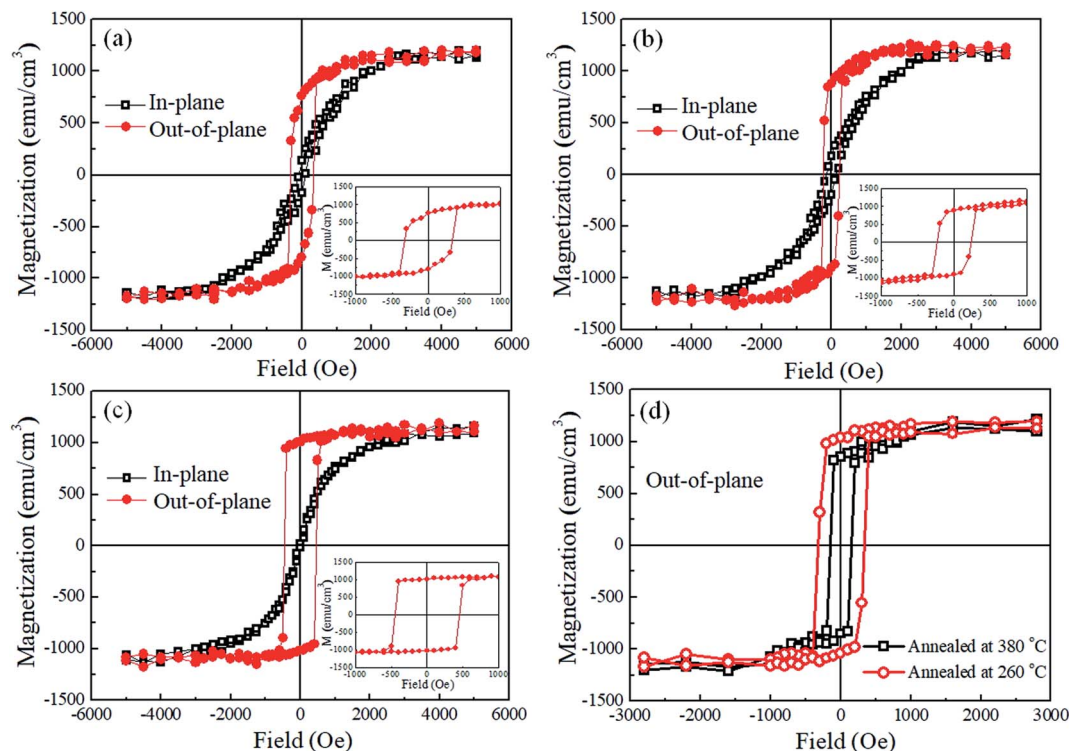
Fig. 1 Hysteresis loops of multi-layered films measured at room temperature: (a) Pt/Co/Pt, (b) Ta/Pt/Co/Pt-4, and (c) Ta/Pt/Co/Pt-20; the insets are the enlarged views of the out-of-plane hysteresis loops. (d) Out-of-plane hysteresis loops of Ta/Pt/Co/Pt-20 annealed at 260 °C and 380 °C, measured at room temperature.

a sputtering power of 8 W displays an ultra-high resistivity ($\rho = 3.9 \times 10^5 \ \mu\Omega$ cm), exhibiting three orders of higher magnitude than that of the β-Ta. This ultra-high resistivity of the Ta film could be related to the experimental conditions, such as low sputtering power, high sputtering Ar pressure, and ultra-large target-to-substrate distance.[41–43] (ii) Fig. 2(a) and (b) present the XRD patterns of the Ta/Pt/Co/Pt samples. (002), (202) and (410) diffraction peaks corresponding to β-Ta were observed for the Ta/Pt/Co/Pt-4 sample [see Fig. 2(a)], while no Ta diffraction peak was observed for the Ta/Pt/Co/Pt-20 sample [see Fig. 2(b)], indicating that Ta is an amorphous structure in the Ta/Pt/Co/Pt-20 sample. These results are consistent with the resistivity data discussed above. In our experiment, the ultra-high resistivity of the Ta film is probably attributed to the amorphous structure and entrapment of Ar ions in the Ta film, resulting from a low deposition rate and high sputtering Ar pressure. For metal films grown by a magnetron sputtering technology, low sputtering power, high sputtering Ar pressure, and large target-to-substrate distance can effectively reduce the deposition rate of metals.[42,43] The growth rate of the ultra-high resistance Ta is ~0.0025 nm s^{-1}, which is far less than that of the β-Ta film (~0.0115 nm s^{-1}). This low growth rate as well as high Ar pressure result in an amorphous structure of Ta, characterized by XRD pattern, as shown in Fig. 2(b). Also, the high-resolution transmission electron microscopy and fast Fourier transform (FFT) exhibited that the Ta layer is an amorphous state in our previous publication.[18] On the other hand, the entrapment of Ar ions in the sputtering process is mainly due to the incorporation of Ar

ions.[42] Owing to the low sputtering power and high sputtering Ar pressure, the mean free path of the molecules is so small that the low-energy Ar ions will undergo numerous collisions with gas molecules in the sputtering chamber and lose energy with a large target-to-substrate distance, causing some Ar atoms doped into the Ta film.[42,44] In addition, the Ar element in the ultra-high resistivity Ta film was detected via XPS, as shown in the inset of Fig. 2(b). The charge-shifted spectrum was corrected using the maximum of the adventitious C 1s signal at 284.8 eV. A distinct binding energy peak of Ar 2p at 241.3 eV indicates the formation of the Ar impurity in the Ta film. One note should be made about the surface roughness of Ta films. From Fig. 2(c) and (d), one can see that the β-Ta and ultra-high resistivity Ta films have smooth surfaces with a roughness of 0.236 nm and 0.269 nm, respectively. Thus, both can be used as underlayers to grow Pt/Co/Pt multi-layered films.

Fig. 3 shows the anomalous Hall curves of the Ta/Pt/Co/Pt-4 and Ta/Pt/Co/Pt-20 films with different currents under a perpendicular magnetic field, using the configuration shown in the inset of Fig. 3(a). It can be seen that both Hall loops exhibit high squareness and the values of the anomalous Hall resistance (R_H) remain constant with the change in current, suggesting that the anomalous Hall effect in the Ta/Pt/Co/Pt samples is not very sensitive to heating. The coercivity of the Ta/Pt/Co/Pt-20 multi-layered film reaches 210 Oe, which is significantly higher than that of Ta/Pt/Co/Pt-4 (about 96 Oe), indicating that the multi-layered film with the ultra-high resistivity Ta underlayer possesses stronger PMA and better thermal
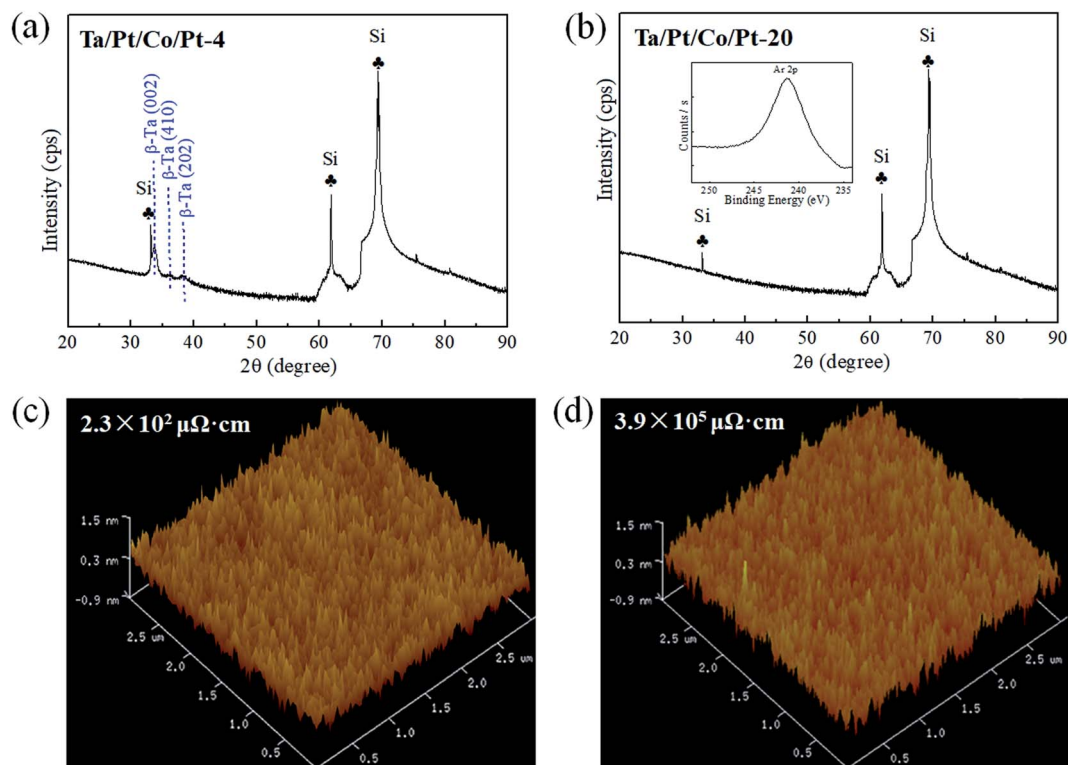
Fig. 2 The XRD patterns for Ta/Pt/Co/Pt-4 (a) and Ta/Pt/Co/Pt-20 (b) multi-layered films. AFM images for the β-Ta film with $\rho = 2.3 \times 10^2$ μΩ cm (c) and the ultra-high resistivity Ta film with $\rho = 3.9 \times 10^5$ μΩ cm (d). The inset of (b) shows the Ar 2p core-level XPS spectrum of the Ta/Pt/Co/Pt-20 film.

stability. This result is consistent with the coercivity variation trend of the magnetic hysteresis loops in Fig. 1(b) and (c). In case of the Ta/Pt/Co/Pt-20 film, the presence of the ultra-high resistivity Ta underlayer improves the electron additional scattering at the amorphous Ta/Pt interface, thereby effectively enhancing the PMA and thermal stability of the film.[45] Meanwhile, the ultra-high resistivity reduces the partial current of the Ta layer in the multi-layered film and increases the partial current in the magnetic metal Co layer.

To further analyze the influence of ultra-high resistivity on the PMA of the films, the planar Hall effect of the Ta/Pt/Co/Pt-4 and Ta/Pt/Co/Pt-20 films was measured and the value of H_{an} was calculated. As shown in the inset of Fig. 3(a), in our measurements an in-plane external magnetic field (H_{ext}) was applied within the x–z plane at a small angle of 7° with respect to the x axis. Fig. 4 shows the planar Hall curves of Ta/Pt/Co/Pt-4 and Ta/Pt/Co/Pt-20 at different temperatures with the small current of 0.1 mA. The magnetic moment of the magnetic metal Co
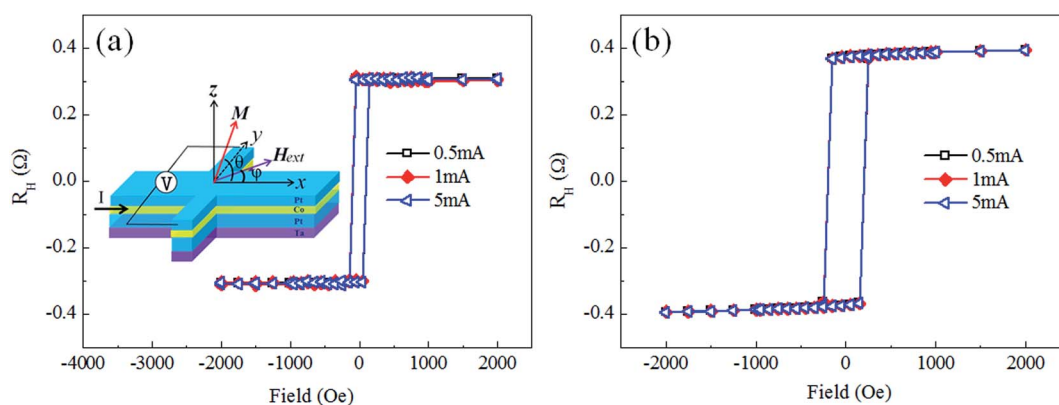

Fig. 3 The anomalous Hall curves of (a) Ta/Pt/Co/Pt-4 and (b) Ta/Pt/Co/Pt-20 samples. The inset shows the configuration of anomalous Hall and plane Hall measurements on the multi-layered Hall bar structure. The magnetic field (H_{ext}) and the current (I, along the x axis) are indicated; and φ is the angle between H_{ext} and the x axis; θ is the angle between the magnetization vector M and the x axis.
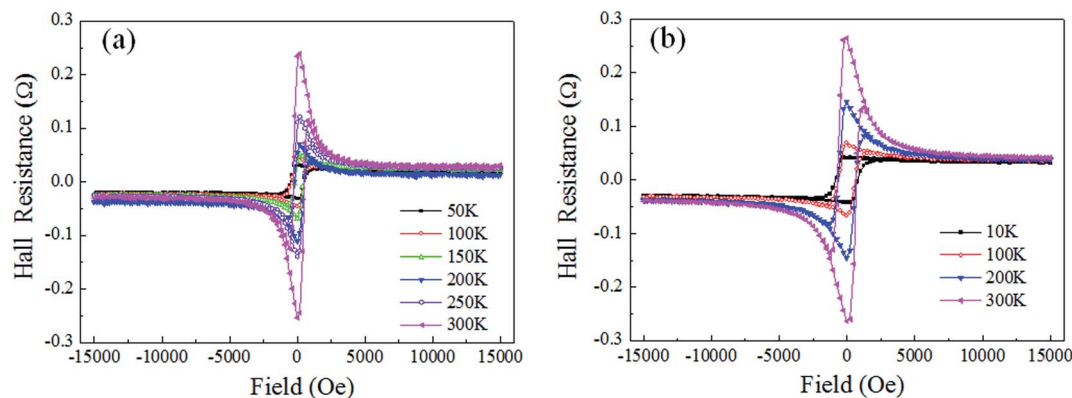
Fig. 4 The plane Hall curves of Ta/Pt/Co/Pt-4 (a) and Ta/Pt/Co/Pt-20 (b) samples.

gradually rotates back and forth between the out-of-plane and in-plane directions when H_{ext} is swept along the x axis between ± 1.5 T. The planar Hall resistance (R_{PH}) approaches a fixed value at high fields, suggesting that the direction of the magnetic moment is nearly parallel to the film plane. The changing trend of R_{PH} with temperature is similar to that reported by Hao et al. in the Ta/CoFeB/MgO structure.[46] H_{an} at different temperatures can be calculated according to the following equation when a current of nearly zero is applied to the Hall bar:[18,46]

$$H_{ext} = H_{an} \sin(\theta)\cos(\theta)/\sin(\theta - \varphi) \qquad (1)$$

where θ is the angle between the sample film plane and the magnetic moment, and φ is the angle between the external magnetic field and film plane, as shown in the inset of Fig. 3(a). According to Fig. 4, H_{ext} can be plotted as a function of $\sin(\theta)\cos(\theta)/\sin(\theta - \beta)$. A complete linear relationship is observed at different temperatures, as expected from eqn (1). The values of H_{an} can be obtained from the slopes of the fitted line.[11,46] Fig. 5 shows the values of H_{an} of the two samples with temperatures. It
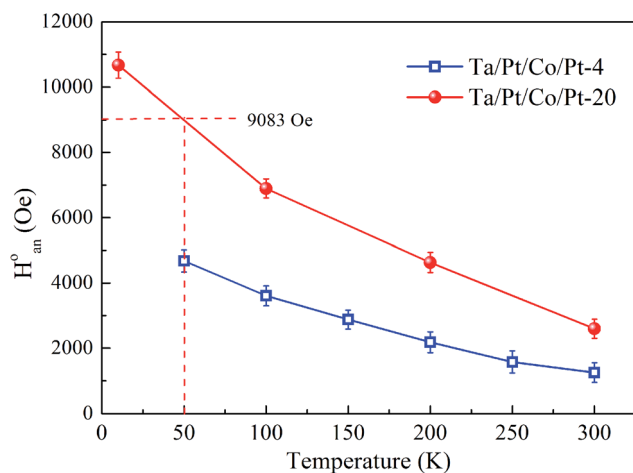
can be seen that H_{an} increases with the decrease in temperature, but the values of the Ta/Pt/Co/Pt-20 sample remain larger than that of the Ta/Pt/Co/Pt-4 sample over the entire temperature range. H_{an} of the Ta/Pt/Co/Pt-20 sample reaches 1.1 T at 10 K. The estimated value of H_{an} of the Ta/Pt/Co/Pt-20 at 50 K is 9083 Oe, which is nearly twice as high as that of the Ta/Pt/Co/Pt-4 sample ($H_{an} = \sim 4620$ Oe). These results confirm that the insertion of the ultra-high resistivity Ta underlayer greatly improves the PMA and thermal stability of the Pt/Co/Pt film. It is worth noting that in the Ta/Pt/Co/Pt multi-layered structure the upper and lower layers adjacent to the magnetic metal Co are both Pt. When current is applied, the spin direction of the spin-polarized current injected from the upper and lower heavy metal Pt layers are opposite due to same signs of the spin Hall angle in the two Pt layers; then, the torque would almost cancel each other out. Thus, the magnetization switching was not observed in our experiment.

Conclusions

In conclusion, the influence of an ultra-high resistivity Ta underlayer on PMA and thermal stability in Ta/Pt/Co/Pt heterostructures were investigated. An optimized amorphous Ta film was obtained at a high sputtering Ar pressure, low sputtering power, and large target-to-substrate distance, exhibiting an ultra-high resistivity ($\rho = 3.9 \times 10^5$ $\mu\Omega$ cm) of three orders of magnitude higher than that of β-Ta. The Ta underlayer having the ultra-high resistivity increases the additional electron scattering in the Ta/Pt interface, thereby effectively improving the PMA and thermal stability of the magnetic layer. The H_{an} reaches a maximum of 1.1 T at 10 K. These results reveal the inherent relationship between the high resistance heavy metal underlayer and PMA, and provide a new approach to improve the PMA and SOT for heavy metal/magnetic metal multi-layered film structures.

Fig. 5 The values of H_{an} of the Ta/Pt/Co/Pt-4 and Ta/Pt/Co/Pt-20 samples at different temperatures ranging from 10 K to 300 K.

Conflicts of interest

There are no conflicts to declare.

Acknowledgements

References

1   I. M. Miron, K. Garello, G. Gaudin, P. J. Zermatten, M. V. Costache, S. Auffret, S. Bandiera, B. Rodmacq, A. Schuhl and P. Gambardella, *Nature*, 2011, **476**, 189–193.
2   S. Ikeda, K. Miura, H. Yamamoto, K. Mizunuma, H. D. Gan, M. Endo, S. Kanai, J. Hayakawa, F. Matsukura and H. Ohno, *Nat. Mater.*, 2010, **9**, 721–724.
3   W.-G. Wang, M. Li, S. Hageman and C. L. Chien, *Nat. Mater.*, 2011, **11**, 64–68.
4   S. H. Yang, K. S. Ryu and S. Parkin, *Nat. Nanotechnol.*, 2015, **10**, 221–226.
5   M. Tang, W. Li, Y. Ren, Z. Zhang, S. Lou and Q. Y. Jin, *RSC Adv.*, 2017, **7**, 5315.
6   S. Mangin, D. Ravelosona, J. A. Katine, M. J. Carey, B. D. Terris and E. E. Fullerton, *Nat. Mater.*, 2006, **5**, 210–215.
7   H. Meng and J.-P. Wang, *Appl. Phys. Lett.*, 2006, **88**, 172506.
8   S. Yakata, H. Kubota, Y. Suzuki, K. Yakushiji, A. Fukushima, S. Yuasa and K. Ando, *J. Appl. Phys.*, 2009, **105**, 07D131.
9   L. J. Zhu, S. H. Nie, K. K. Meng, D. Pan, J. H. Zhao and H. Z. Zheng, *Adv. Mater.*, 2012, **24**, 4547–4551.
10 N. Nagaosa and Y. Tokura, *Nat. Nanotechnol.*, 2013, **8**, 899–911.
11 L. Q. Liu, C.-F. Pai, Y. Li, H. W. Tseng, D. C. Ralph and R. A. Buhrman, *Science*, 2012, **336**, 555–558.
12 M. Tang, R. Ramaswamy, H. Yang, H. Yang, W. Fan, Z. Shi, S. Zhou and X. Qiu, *Appl. Phys. Lett.*, 2018, **113**, 222406.
13 X. Qiu, Z. Shi, W. Fan, S. Zhou and H. Yang, *Adv. Mater.*, 2018, **30**, 1705699.
14 S. Chen, J. Yu, Q. Xie, X. Zhang, W. Lin, L. Liu, J. Zhou, X. Shu, R. Guo, Z. Zhang and J. Chen, *ACS Appl. Mater. Interfaces*, 2019, **11**, 30446–30452.
15 L. Q. Liu, O. J. Lee, T. J. Gudmundsen, D. C. Ralph and R. A. Buhrman, *Phys. Rev. Lett.*, 2012, **109**, 096602.
16 P. Li, T. Liu, H. C. Chang, A. Kalitsov, W. Zhang, G. Csaba, W. Li, D. Richardson, A. DeMann, G. Rimal, H. Dey, J. S. Jiang, W. Porod, S. B. Field, J. K. Tang, M. C. Marconi, A. Hoffmann, O. Mryasov and M. Z. Wu, *Nat. Commun.*, 2016, **7**, 12688.
17 G. Y. Shi, C. H. Wan, Y. S. Chang, F. Li, X. J. Zhou, P. X. Zhang, J. W. Cai, X. F. Han, F. Pan and C. Song, *Phys. Rev. B*, 2017, **95**, 104435.
18 R. Wang, Z. Y. Xiao, H. H. Liu, Z. Y. Quan, X. Zhang, M. M. Wang, M. Z. Wu and X. H. Xu, *Appl. Phys. Lett.*, 2019, **114**, 042404.
19 C. Zhang, S. Fukami, K. Watanabe, A. Ohkawara, S. DuttaGupta, H. Sato, F. Matsukura and H. Ohno, *Appl. Phys. Lett.*, 2016, **109**, 192405.
20 W. Skowroński, M. Cecot, J. Kanak, S. Ziętek, T. Stobiecki, L. Yao, S. van Dijken, T. Nozaki, K. Yakushiji and S. Yuasa, *Appl. Phys. Lett.*, 2016, **109**, 062407.
21 C.-F. Pai, L. Q. Liu, Y. Li, H. W. Tseng, D. C. Ralph and R. A. Buhrman, *Appl. Phys. Lett.*, 2012, **101**, 122404.
22 Q. Hao, W. Z. Chen and G. Xiao, *Appl. Phys. Lett.*, 2015, **106**, 182403.
23 G. W. Kim, A. S. Samardak, Y. J. Kim, I. H. Cha, A. V. Ognev, A. V. Sadovnikov, S. A. Nikitov and Y. K. Kim, *Phys. Rev. Appl.*, 2018, **9**, 064005.
24 Y. Takeuchi, C. L. Zhang, A. Okada, H. Sato, S. Fukami and H. Ohno, *Appl. Phys. Lett.*, 2018, **112**, 192408.
25 M. Cecot, Ł. Karwacki, W. Skowroński, J. Kanak, J. Wrona, A. Żywczak, L. Yao, S. van Dijken, J. Barnaś and T. Stobiecki, *Sci. Rep.*, 2017, **7**, 968.
26 G. Allen, S. Manipatruni, D. E. Nikonov, M. Doczy and I. A. Young, *Phys. Rev. B: Condens. Matter Mater. Phys.*, 2015, **91**, 144412.
27 J. Kim, J. Sinha, S. Mitani, M. Hayashi, S. Takahashi, S. Maekawa, M. Yamanouchi and H. Ohno, *Phys. Rev. B: Condens. Matter Mater. Phys.*, 2014, **89**, 174424.
28 X. P. Qiu, P. Deorani, K. Narayanapillai, K. S. Lee, K. J. Lee, H. W. Lee and H. Yang, *Sci. Rep.*, 2014, **4**, 4491.
29 D. Li, B. S. Cui, T. Wang, J. J. Yun, X. B. Guo, K. Wu, Y. L. Zuo, J. B. Wang, D. Z. Yang and L. Xi, *Appl. Phys. Lett.*, 2017, **110**, 132407.
30 B. S. Cui, S. W. Chen, D. Li, J. J. Yun, X. B. Guo, K. Wu, X. Zhang, Y. P. Wang, Y. L. Zuo, M. Z. Gao and L. Xi, *Appl. Phys. Express*, 2018, **11**, 013001.
31 H. L. Ju, P. P. Xiang, W. Wang and B. H. Li, *Acta Phys. Sin.*, 2015, **64**, 197501.
32 S. P. Bommanaboyena and M. Meinert, *Appl. Phys. Lett.*, 2017, **111**, 042407.
33 S. Ikeda, K. Miura, H. Yamamoto, K. Mizunuma, H. D. Gan, M. Endo, S. Kanai, J. Hayakawa, F. Matsukura and H. Ohno, *Nat. Mater.*, 2010, **9**, 721–724.
34 H. Sato, M. Yamanouchi, S. Ikeda, S. Fukami, F. Matsukura and H. Ohno, *Appl. Phys. Lett.*, 2012, **101**, 022414.
35 B. Cui, C. Song, G. A. Gehring, F. Li, G. Wang, C. Chen, J. Peng, H. Mao, F. Zeng and F. Pan, *Adv. Funct. Mater.*, 2015, **25**, 864–870.
36 Z. Y. Xiao, F. Zhang, M. A. Farrukh, R. Wang, G. W. Zhou, Z. Y. Quan and X. H. Xu, *J. Mater. Sci.*, 2019, **54**, 9017–9024.
37 O. J. Lee, L. Q. Liu, C. F. Pai, Y. Li, H. W. Tseng, P. G. Gowtham, J. P. Park, D. C. Ralph and R. A. Buhrman, *Phys. Rev. B: Condens. Matter Mater. Phys.*, 2014, **89**, 024418.
38 S. Chen, J. Zhou, W. Lin, J. Yu, R. Guo, F. Poh, D. Shum and J. S. Chen, *J. Phys. D: Appl. Phys.*, 2018, **51**, 055006.
39 P. Sethi, S. Krishnia, S. H. Li and W. S. Lew, *J. Magn. Magn. Mater.*, 2017, **426**, 497.
40 M. Furuta, Y. Liu, H. Sepehri-Amin, K. Hono and J. G. Zhu, *J. Appl. Phys.*, 2017, **122**, 113901.
41 M. Grosser and U. Schmid, *Thin Solid Films*, 2009, **517**, 4493–4496.
42 W. W. Y. Lee, *J. Appl. Phys.*, 1971, **42**, 4366.
43 E. Krikorian and R. J. Sneed, *J. Appl. Phys.*, 1966, **37**, 3674.
44 E. V. Kornelsen, *Can. J. Phys.*, 1964, **42**, 364–381.
45 N. Ryzhanova, A. Vedyayev, A. Pertsova and B. Dieny, *Phys. Rev. B: Condens. Matter Mater. Phys.*, 2009, **80**, 024410.
46 Q. Hao and G. Xiao, *Phys. Rev. B: Condens. Matter Mater. Phys.*, 2015, **91**, 224413.